coatings

MDPI

Article

Preparation of ZnO Thick Films Activated with UV-LED for Efficient H_2S Gas Sensing

Claudio Martínez-Pacheco [1], José Luis Cervantes-López [1], Antonia del Rocío López-Guemez [1], Angélica Silvestre López-Rodríguez [1], Pio Sifuentes-Gallardo [1], Juan Carlos Díaz-Guillen [2] and Laura Lorena Díaz-Flores [1,*]

[1] División Académica de Ingeniería y Arquitectura, Universidad Juárez Autónoma de Tabasco, Km 1 Carretera Cunduacán-Jalpa de Méndez, Col. La Esmeralda, Cunduacán CP 86690, Tabasco, Mexico; 202d20001@alumno.ujat.mx (C.M.-P.); jose.cervantes@ujat.mx (J.L.C.-L.); antonia.lopez@ujat.mx (A.d.R.L.-G.); angelica.lopez@ujat.mx (A.S.L.-R.); pio.sifuentes@ujat.mx (P.S.-G.)

[2] Consejo Nacional de Humanidades, Ciencias y Tecnologías—InnovaBienestar de México, Ciencia y Tecnología 790, Saltillo CP 25290, Coahuila, Mexico; jcarlos@comimsa.com

* Correspondence: laura.diaz@ujat.mx

Abstract: In this work, ZnO thick films were synthesized via two simple and easy methods, mechanochemical synthesis and screen-printing deposition. The ZnO powders were obtained through milling at low temperature with milling times of 20, 40, and 60 min. The ZnO thick films were fabricated by depositing 10 cycles of ZnO inks onto glass substrates. The characterization of ZnO thick films revealed a thickness ranging from 4.9 to 5.4 µm with a surface roughness between 85 and 88 nm. The structural analysis confirmed a hexagonal wurtzite crystalline structure of ZnO, both in powders and in thick films, with a preferred orientation on the (002) and (101) planes. Nanostructures with sizes ranging from 36 to 46 nm were observed, exhibiting irregular agglomerated shapes, with an energy band found between 2.77 and 3.02 eV. A static experimental set up was fabricated for gas sensing tests with continuous UV-LED illumination. The ZnO thick films, well adhered to the glass substrate, demonstrated high sensitivity and selectivity to H_2S gas under continuous UV-LED illumination at low operating temperatures ranging from 35 to 80 °C. The sensitivity was directly proportional, ranging from 3.93% to 22.40%, when detecting H_2S gas concentrations from 25 to 600 ppm.

Keywords: zinc oxide; screen printing; mechanochemical method; nanostructures; UV-LED illumination

Citation: Martínez-Pacheco, C.; Cervantes-López, J.L.; López-Guemez, A.d.R.; López-Rodríguez, A.S.; Sifuentes-Gallardo, P.; Díaz-Guillen, J.C.; Díaz-Flores, L.L. Preparation of ZnO Thick Films Activated with UV-LED for Efficient H_2S Gas Sensing. *Coatings* **2024**, *14*, 693. https://doi.org/10.3390/coatings14060693

Academic Editor: Chang Kwon Hwangbo

Received: 26 April 2024
Revised: 19 May 2024
Accepted: 30 May 2024
Published: 1 June 2024

1. Introduction

Monitoring analytes, such as contaminants, explosives, and heavy metal ions, is important for the protection of human beings, considering disease identification and environmental protection [1]. Among the most dangerous gaseous analytes are carbon monoxide (CO) and sulfur dioxide (SO_2), produced by combustion of fossil fuels [2]; ammonia (NH_3), generated by industrial and agricultural activities [3]; and hydrogen sulfide (H_2S), a colorless, toxic, corrosive, and flammable gas produced in oil and gas industry processes such as petroleum refining, natural gas sweetening, and the reduction of sulfates from hydrocarbons in wastewater. Its toxicity can cause damage to the central nervous system in a very short period of time [4]. Short-term exposure (10 min) to H_2S gas has a limit of 15 ppm, and long-term exposure (8 h) has been set at 10 ppm. H_2S gas can cause instant death when inhaling a concentration of 1000 to 2000 ppm [5]. However, exposure to concentrations as low as 2 ppm can cause nausea and headaches, and at higher concentrations of 50 to 100 ppm, it can affect the respiratory tract and cause digestive problems. For these reasons, there is a need to monitor H_2S gas at concentrations lower than 100 ppm [6].

For this purpose, it is essential to have accurate electronic devices for real-time gas monitoring, which enables timely protection for individuals. In this regard, over the past

20 years, research has been conducted on gas sensors based on semiconductor nanomaterials, which are the most used gas sensors in the world. Currently, gas sensitive nanomaterials such as carbon-based materials, semiconductor metal oxides (SMOX), and conductive polymers have been used for gas sensor fabrication [7]. One of the most used conductive polymers is polyaniline, which is generally combined with chitosan to create a polymeric composite [3]. In the other hand, among the most used SMOX in gas sensors fabrication are copper oxide (CuO), tin oxide (SnO_2), nickel oxide (NiO), indium oxide (In_2O_3), tungsten oxide (WO_3), and zinc oxide (ZnO) [8]. The latter, ZnO, is a material obtained through simple methods, and its manufacturing is low cost. It is an n-type semiconductor with a bandgap of ~3.37 eV, an exciton binding energy of 60 meV, and high electron mobility of 400 $cm^2\ V^{-1}s^{-1}$ [9]. It exhibits transparency in the visible spectrum and high reflectivity in the infrared region [10]. These properties allow ZnO to be employed effectively in various electronic and optoelectronic applications such as solar cells, light-emitting diodes, piezoelectric devices, gas sensors (thermal-activated) [11] and gas sensors (UV-activated) [12], among others.

There are several synthesis methods for obtaining ZnO nanostructures with different morphological characteristics and variations in their physical properties, such as the sol–gel method, chemical vapor deposition, hydrothermal method, ball milling (mechanochemical process) [13], carbo-thermal evaporation [14] and electron beam evaporation [15], to name a few. The mechanochemical method has several advantages over other methods such as simplicity, low cost, low time consumption and minimal waste generation processes, capable of producing nanomaterials on a large scale. The mechanochemical method most of the time promotes changes in strain, structure, and morphology that affect the optical and electrical properties of materials [16]. Some drawbacks of the method are the need for high energy and contamination of powder due to steel balls [17].

ZnO films can be prepared on different substrates by means of various facile and low-cost deposition techniques such as drop casting, spin coating, ink jet printing and screen printing [18]. The screen-printing technique is versatile and allows for the cost-effective deposition of thick films on various types of substrates [19]. Despite the large areas that can be deposited with this technique, there are some drawbacks such as relatively thick films formed and high sintering temperatures [20]. In choosing the substrate, it is important to consider that common substrates are resistant to electrical conductivity and inert. Commercially, the following can be found: alumina, quartz, silicon, glass, soda-lime glass [21], fluorine-doped tin oxide (FTO), indium-doped tin oxide (ITO) and aluminum-doped zinc oxide (AZO) [22].

Gas sensors based on ZnO nanostructures often require an external excitation to activate the surface of ZnO and thus accelerate the adsorption/desorption processes of gas molecules. Typically, this activation occurs at high temperatures, between 300 and 500 °C, where a metallic heater is responsible for raising the temperature, which requires advanced energy consumption, about 500 to 5000 mW [23]. Currently, other options to activate a gas sensor are the 2D and 3D microheaters, due to their low energy consumption, which is in the range of 10 to 80 mW and raise the temperature from 0 to 700 °C [24]. On the other hand, high temperatures in this type of sensors can be dangerous, affecting sensor stability, lifetime, and limiting the detection of flammable or explosive gases. Another drawback is the potential interference of water molecules present in the atmosphere, which can be chemisorbed on the surface of ZnO nanostructures [25].

In order to reverse these disadvantages in gas detection, surface modifications, as well as doping and light activation of ZnO nanostructures, have been carried out, improving sensitivity and selectivity at room temperature [26]. An increase in sensitivity at room temperature can be obtained with UV-photoactivation, using low energy consumption UV-LEDs (UV-light-emitting diodes). UV-LEDs are able to excite the surface of a chemiresistive sensor with low energy consumption, about 50 to 500 mW for optimum operating conditions. For this reason, the use of UV-LEDs is attractive for the development of highly sensitive gas sensors with low energy consumption [12].

In the present work, the fabrication of gas sensor based on nanostructured ZnO thick films on a glass substrate is described. For this purpose, the fabrication of ZnO thick films was carried out in three steps, using two simple and easy methods: mechanochemical synthesis and screen-printing film deposition. The first step was the synthesis of ZnO powders with three different milling times by mechanochemical synthesis. The next step was the ZnO thick film deposition by means of the screen-printing technique. And the final step was the thermal treatment of the ZnO thick films. The electrical resistance of the ZnO thick film sensor upon exposure to H_2S gas and other species was measured. It was compared to the response of ZnO thick film sensors towards 25 to 600 ppm of H_2S gas in a low operating temperature range from 35 to 80 °C with and without continuous UV-LED illumination activation. The gas sensing test towards 600 ppm of H_2S gas at 35 °C, the lowest operating temperature tested, showed that the ZnO sensor activated with continuous UV-LED illumination improved its response with an increase of 88%. However, when combining continuous UV-LED illumination and a low operating temperature of 65 °C, the response of the ZnO sensor improved even more, since it increased up to 116%. This improvement in the sensitivity of the ZnO sensor was carried out with continuous UV-LED illumination activation and low operating temperature with low energy consumption (nominal energy consumption of UV-LED is 55 mW). The characteristics of the nanostructured ZnO thick films, such as small crystallite size, preferential nanostructure growth orientation in the (002) plane, surface roughness and continuous UV-LED illumination, contributed to the improvement of the ZnO sensor response. These activities allowed us to study the optimal ZnO thick film fabrication conditions required for gas sensing and to validate the feasibility of using this type of sensors indoors or outdoors near sources emitting H_2S gas or dynamic equipment releasing such vapors through sour gas handling.

2. Materials and Methods

For the synthesis of ZnO powders and fabrication of ZnO thick films, the reagents used were zinc chloride [$ZnCl_2$] (J.T. Baker, Phillipsburg, NJ, USA, 97.0%–100.5%), sodium carbonate [Na_2CO_3] (J.T. Baker, 99.5%), sodium chloride [NaCl] (J.T. Baker, 99%), ethanol [C_2H_6O] (Meyer, Vallejo, CA, USA, 99.5%), terpineol [$C_{10}H_{18}O$] (Aldrich, St. Louis, MI, USA, mixture of isomers, anhydrous), and ethylcellulose [$C_{23}H_{24}N_6O_4$] (Sigma-Aldrich, St. Louis, MI, USA, 5% in toluene/ethanol 80:20 (lit.), extent of labeling: 48% ethoxyl). All reagents were used as they come in their trademark.

2.1. Synthesis of ZnO Powders by Mechanochemical Processing

The first step of manufacturing ZnO thick films consisted of obtaining three ZnO powder samples, which are the basis of the ink for the next stage. The precursor reagents were placed in the 100 mL stainless steel vials of the Spex@ 8000D Mixer/Mill high-energy mill, Thomas Scientific, Swedesboro, NJ, USA, which has a 1/3 Hp motor running at 1725 rpm, a clamp speed of 1060 cycles per minute, and a range of motion of 2 1/3 inches (5.9 cm) back-and-forth and 1 inch (2.5 cm) side-to-side. The milling cycles were performed, consisting of three runs with different times: 20, 40 and 60 min at 1725 rpm. Samples were named 20, 40 and 60 min, respectively. The synthesis of ZnO was carried out following the chemical reaction (Equation (1)):

$$ZnCl_2 + Na_2CO_3 + 8NaCl \rightarrow ZnO + CO_2 + 10NaCl \quad (1)$$

After the milling process, to remove NaCl residues from material, the ZnO powders underwent a selective leaching process, using distilled water as dissolving agent and ultrasonic treatment for 1 h. Finally, a calcination step was performed on the obtained powders at 400 °C for 2 h.

2.2. ZnO Screen-Printed Thick Films Preparation

The second step of the process was the preparation of suspensions of the ZnO nanoparticles. The coatings were carried out on a AT-45FA screen printing equipment, ATMA,

Taoyuan City, Taiwan. For the fabrication of the ZnO thick films, three separate suspensions were prepared, consisting of 5 g of ZnO and 10 mL of ethanol. Subsequently, 4.06 g of terpineol were added, continuing again with an ultrasonic treatment for 30 min. Finally, a binder was added to the suspensions, 0.325 g of ethylcellulose dissolved in 12 mL of ethanol, and this solution was heated to 60 ° C while stirring for 1.5 h. The ZnO paste was used to coat the glass substrates, performing 10 deposition cycles on each substrate, using a 90T mesh (56 μm aperture) and a position angle of 0° in 2θ. Between each layer, drying was carried out at 125 ° C for 10 min. When the coating process was finished, the material was annealed in a muffle at 450 ° C for 1 h. ZnO thick films were labeled Z-20, Z-40 and Z-60, respectively. As can be observed, this process is highly reproducible. The thickness of the ZnO thick films was measured by using a profilometer. The average thickness of ZnO thick films ranged from 4.9 to 5.4 μm.

2.3. ZnO Thick Films Characterization

Crystallographic structures of materials were measured by X-ray diffraction (XRD) using a D8 Advance diffractometer, Bruker, Madison, WI, USA, with Cu Kα1 (λ = 0.15406 nm) operating at 40 kV and 40 mA and collecting from 10° to 80° (2θ). The surface morphology was observed by using a JSM-7600F Scanning Electron Microscope, JEOL, Peabody, MA, USA. The experiments were carried out at an accelerating voltage of 15 kV and working distance of 8 mm. The surface topography was measured by using an Confocal Raman integrated with Atomic Force Microscope (AFM) Alpha 300, Witec, Ulm, Germany. The measurement was conducted in an area of 100 μm^2 (10 μm width and 10 μm height). The vibrational modes of the lattice were studied by Raman spectroscopy, using a Confocal Raman integrated with Atomic Force Microscope (AFM) Alpha 300, Witec, Ulm, Germany with a 400 nm excitation laser. The optical evaluation of the ZnO thick films was carried out by measuring optical absorption with a 1280 Ultraviolet-Visible (UV-Vis) spectrophotometer, Shimadzu, Columbia, MD, USA, at a wavelength from 300 to 800 nm, in absorbance mode. The thickness of the thick films was measured by contact profilometry technique using a Tencor D-500 profilometer, KLA, San Diego, CA, USA, at a 0.03 mms^{-1} in the sweep speed with 3 mm on linear path on ZnO thick film. Electrical resistivity was determined using the four-points probe technique with a Sourcemeter 2420 equipment, Keithley-Tektronix, Beaverton, OR, USA, with the following specifications: measure voltage from 1 μV to 63.3V and source current from 500 pA to 3.15 A. The adhesion properties were evaluated by means of the cross-sectional adhesive tape test, according to the ASTM D3359-22 standard [27].

2.4. ZnO Gas Sensor Fabrication and Gas Measurement Setup

The ZnO gas sensor was fabricated through the deposition of a pair of silver electrodes by the screen-printing technique using a conductive silver paste. For gas sensing tests, a homemade static gas measurement setup was fabricated, comprising a ZnO gas sensor, UV-LED (390 nm = 3.2 eV; nominal energy consumption: 55 mW), gas chamber with 550 mL volume and data acquisition system (DAS) interfaced with computer for recording the electrical resistance in the presence of ambient air and in the presence of target gas concentrations. The structure of the ZnO gas sensor and the homemade static gas measurement setup for the gas sensing tests are schematically shown in Figure 1.

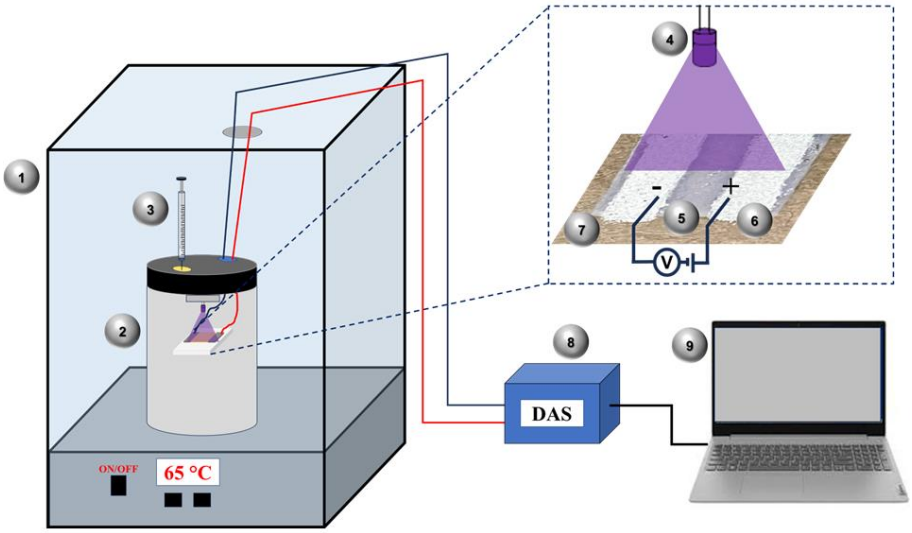

Figure 1. Schematic diagram of a homemade static gas measurement setup. (1) Electric oven with temperature control; (2) gas chamber; (3) precision syringe; (4) UV-LED (390 nm); (5) nanostructured ZnO thick film; (6) Ag electrodes; (7) glass substrate; (8) data acquisition system; (9) portable computer.

The gas sensing tests of the ZnO gas sensors were carried out placing the homemade static gas measurement setup into an electric oven, for controlling the working temperature of a ZnO gas sensor in the range from 35 to 80 °C, considering low temperature under 100 °C. Firstly, the ZnO gas sensor underwent a stabilization process for one hour, maintaining the temperature constant in the presence of ambient air and with the UV-LED on. This process was repeated for each of the temperatures. Secondly, the gas chamber was sealed and a precision syringe was used to inject a given amount of gas under testing, so that the chamber maintained the desired target gas concentration. The volume of injected gas was calculated as follows according to Equation (2) [28]:

$$V_{Inj} = V * C * 10^{-6} * \frac{273 + T_E}{273 + T_C} \quad (2)$$

where V_{Inj} is the volume of gas to be injected (mL), V is the volume of the gas chamber (mL), C is the gas concentration (ppm), T_E is the ambient temperature (°C), and T_C is the gas chamber temperature (°C). The target gas was H_2S and concentrations tested were from 25 to 600 ppm. Finally, when the ZnO gas sensor had enough interaction with the target gas, the gas chamber was opened and the gas was let out. At this time, the ZnO gas sensor interacted with the ambient air. Afterwards, the gas chamber was closed and a new gas concentration was injected into the chamber again. The response and recovery cycle were repeated in static conditions. The UV-LED was on during each response and recovery cycle with an intensity of 1.38 mW/cm^2 for activation of the ZnO gas sensor. Every gas sensing test were performed by applying a fixed bias of 5 V across the silver electrodes and recording the electrical resistance as a function of time by using the data acquisition system. The sensor response (S) is calculated in percentage by the following equation [29]:

$$S = \frac{(R_{air} - R_{gas})}{R_{air}} * 100\% \quad (3)$$

Here, R_{gas} and R_{air} represent the electrical resistance measured by the ZnO sensor during gas and air exposure, respectively. The response time (T_{res}) and recovery time (T_{rec}) are defined as the required time to reach 90% of total change in electrical resistance upon exposure to gas and air, respectively.

3. Results and Discussion

3.1. Structural Analysis of ZnO Thick Films

The diffraction patterns of ZnO powders and ZnO thick films are presented in Figure 2a,b respectively. All samples are polycrystalline, with well-defined signals for the (100), (002), (101), (102), (110), and (103) planes, consistent with the data provided by the ICDD 00-036-1451 card, which is specifically associated with ZnO and its hexagonal wurtzite crystalline structure (a = 0.3249 nm and c = 0.5201 nm). It was observed that the intensity of the diffraction peaks is different, indicating that the growth of ZnO crystals is not uniform across all planes due to an anisotropic growth. Furthermore, the diffraction patterns showed that the intensity of the signals is higher in thick films than in powders. This is due to the nanomaterials manufactured and deposited on substrates being more compacted and ordered in the films and the crystallite size being different, since size is larger in films than in powders.

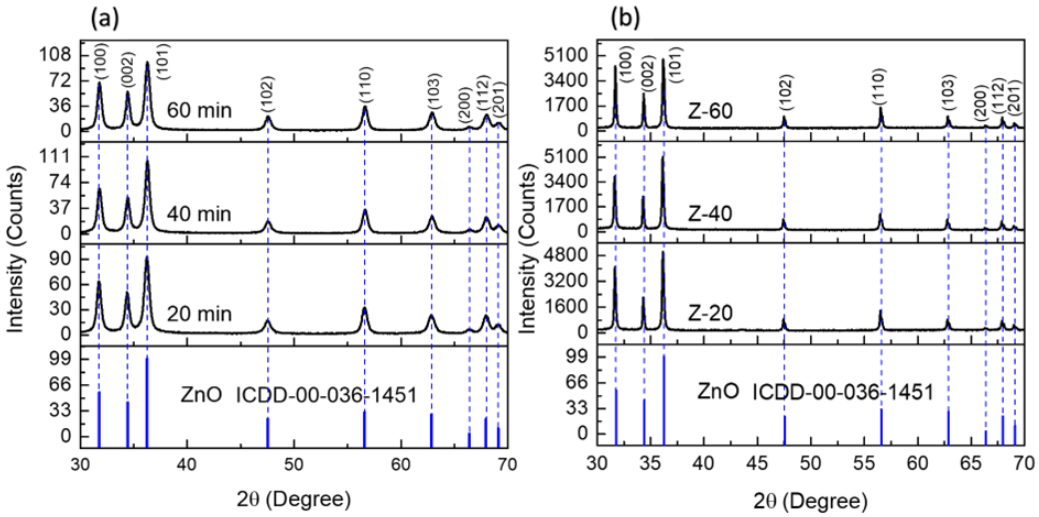

Figure 2. XRD patterns of ZnO nanomaterials. (**a**) ZnO powders obtained by mechanochemical synthesis; (**b**) ZnO thick films deposited by screen-printing technique.

As the milling time is a parameter to select the best process to use in our gas sensors, calculation of lattice parameters (a, c), interplanar spacing (d) and crystallite size (D) were carried out by using the following Equations (4)–(7) [30–33], and physical dimensions of ZnO lattice were obtained:

$$a = \frac{\lambda}{\sqrt{3}\mathrm{Sen}o\theta} \tag{4}$$

$$c = \frac{\lambda}{\mathrm{Sen}o\theta} \tag{5}$$

$$\frac{1}{d_{hkl}^2} = \frac{4}{3}\left(\frac{h^2 + hk + k^2}{a^2}\right) + \frac{l^2}{c^2} \tag{6}$$

$$D = \frac{\kappa\lambda}{B\cos\theta} \tag{7}$$

where λ is the wavelength of the CuKα radiation (0.154 nm), θ is the Bragg angle and k is the shape factor (0.9). B is the full width at half maximum (FWHM) of the X-ray diffraction peak. Table 1 shows the values calculated for the parameters previously described. The parameters were calculated from the position (002) of the ZnO powders and ZnO thick films patterns. The values of the lattice parameters are analogous to the range reported in the literature, parameter a is in the range between 3.2477 and 3.2638 Å, and parameter c is in the range between 5.2026 and 5.2260 Å, coinciding with the values reported in the literature for the bulk wurtzite phase of ZnO [32]. The d spacing values are consistent with the (002) plane from ICDD 00-36-1451 card. This way, we could assume that ZnO powders

and ZnO thick films increase its crystallite size with milling time. This effect is due to the high impact energy during the early stages of milling which effectively cuts down large particles into smaller ones by the fragmentation process, leading to larger crystallite sizes.

Table 1. Structural parameters calculated for ZnO powders and ZnO thick films.

Sample	hkl	D (nm)	a (Å)	c (Å)	d (nm)	FWHM (002)
20 min	002	17.71	3.2497	5.2116	0.2605	0.4692
40 min	002	18.22	3.2477	5.2026	0.2601	0.4562
60 min	002	19.70	3.2477	5.2056	0.2602	0.4220
Z-20	002	32.45	3.2582	5.2212	0.2610	0.2561
Z-40	002	33.69	3.2602	5.2216	0.2611	0.2467
Z-60	002	34.79	3.2562	5.2260	0.2608	0.2389

Since this research focused on ZnO thick film gas sensors, other structural parameters for them were calculated, such as unit cell volume (V), Zn–O bond length (bi), u positional parameter in the wurtzite structure, dislocation density (δ), lattice micro strain (ε) and degree of crystallinity (X_c), by using the specific Equations (8)–(13) given below [30,32,34,35]:

$$V = \frac{\sqrt{3}}{2}a^2c \quad (8)$$

$$bi = uc \quad (9)$$

$$u = \frac{a^2}{3c^2} + 0.25 \quad (10)$$

$$\delta = \frac{1}{D^2} \quad (11)$$

$$\varepsilon = \frac{\beta\cos\theta}{4} \quad (12)$$

$$X_c = \frac{0.24}{\beta_{002}} \quad (13)$$

Table 2 summarizes the values of all of these parameters calculated for ZnO thick films. As can be seen, in this case, the strain values of ZnO nanoparticles decreased as the milling time increased. This uncommon phenomenon of strain reduction can occur with long milling times under ambient conditions, since during that time period, critical values of dislocation density can be reached in the material, promoting strain relaxation [36]. The difference from the ideal value of the positional parameter, u = 3/8 = 0.375, with respect to the values obtained in these ZnO screen-printed thick films, ≈0.3800, makes it clear that the atoms suffered a deviation from their ideal configuration. Also, a change in the length of the Zn-O bonds was observed, with values from 1.983 to 1.984 Å, compared to the ideal value of 1.930 Å; this is due to the strain experienced by the lattice [32]. Specifically, the values of the degree of crystallinity of the ZnO thick films increased from 0.8230 to 0.9824 as the milling time increased. This indicates that a large portion of the material was arranged in an ordered and crystalline structure and represents larger crystallite sizes.

Table 2. Structural parameters calculated for ZnO thick films.

Sample	hkl	V ($Å^3$)	bi (Å)	u	δ ($\times 10^{15}$ m^{-2})	ε (10^{-3})	X_c
Z-20	002	48.01	1.983	0.3798	1.11	1.07	0.8230
Z-40	002	48.06	1.984	0.3800	1.06	1.03	0.9207
Z-60	002	47.97	1.982	0.3799	1.02	1.00	0.9824

Also, the texturing of ZnO thick films was calculated by the texture coefficient (TC), through Equation (14) [37]:

$$T_{c(hkl)} = \frac{I_{(hkl)}/I^0_{(hkl)}}{\sum\left(\frac{I_{(hkl)}}{I^0_{(hkl)}}\right)} \quad (14)$$

where $I_{(hkl)}$ are the measured diffraction intensities obtained from the materials and $I^0{}_{(rhkl)}$ are the intensities of the XRD reference (ICDD 00-36-1451). The texture coefficient calculated for the crystallographic planes (100), (002), (101), (102), (110), and (103) are shown in Table 3. However, the highest peaks in XRD patterns were (100), (002) and (101) planes for all samples. The TC calculation shows that the growth-preferred orientation was along the (002) plane and its values varied from 0.1931 to 0.2043. This preferential growth along the c-axis benefits ZnO thick films for gas sensor applications because it promotes continuous electron transfer [38].

Table 3. Texture coefficient calculated for ZnO thick films.

Sample	(100)	(002)	(101)	(102)	(110)
Z-20	0.1994	0.2043	0.1697	0.1163	0.1804
Z-40	0.1859	0.1931	0.1671	0.1249	0.1842
Z-60	0.1896	0.1969	0.1667	0.1377	0.1702

ZnO thick films were characterized by X-ray diffraction after 12 months of aging, and the hexagonal wurtzite crystalline structure of ZnO was observed. This confirms the stability of the crystalline structure of ZnO and films.

3.2. Raman Analysis of ZnO Lattice

Raman spectra of ZnO thick films at three milling times are shown in Figure 3, where all the samples present four intense and defined signals at 100, 333, 438 and 580 cm^{-1}. These signals are characteristic vibrational modes of ZnO, confirming the results obtained in X-ray diffraction and elemental microscopy analysis. The peak located at 100 cm^{-1} belongs to the low frequency E_{2L} mode, associated with the vibration of the Zn in lattice, while the peak located at 438 cm^{-1} corresponds to the high frequency E_{2H} mode linked to movements of oxygen atoms in the ZnO lattice. The difference in intensities in the E_{2H} vibrational mode is associated with the quality of crystal growth between the samples [39]. The peak located at 333 cm^{-1} is a second-order E_{2H}-E_{2L} vibrational mode arising from photons in the wurtzite limited zone. Finally, the signal at 580 cm^{-1} is an E_1 (LO) mode and is caused by oxygen vacancy defects in ZnO [16,39,40]. The results indicate that the three milling times generate wurzite-type nanostructures with high crystalline quality.

3.3. Morphological Identification and Thickness Measurement

Figure 4a,d,g show SEM images of ZnO nanostructures synthesized by the three milling times by mechanochemical synthesis and the screen-printing deposition technique. The surface of ZnO thick film showed a homogeneous growth of nanostructures, where the morphology identified corresponded to well-shaped nanograins, and it was observed that they clustered together forming agglomerates with high surface density, confirming the anisotropic growth of the ZnO nanograins observed in the XRD patterns.

The average values of ZnO nanograin sizes increased as the milling time was extended. Figure 4b,e,h show the size distribution of ZnO nanograins. The values were 36 ± 7, 44 ± 7 and 46 ± 8 nm for Z-20, Z-40 and Z-60, respectively. To confirm the above mentioned, X-ray energy dispersive spectra (EDS) of ZnO thick films is presented in Figure 4c,f,i, which show the presence of the elements Zn and O confirming the formation of ZnO. The formation of larger ZnO nanograins with an increase in milling time can be attributed to the overlapping of smaller ones or the effect of agglomeration of ZnO nanograins by the accumulation of high energy during the milling process [41].

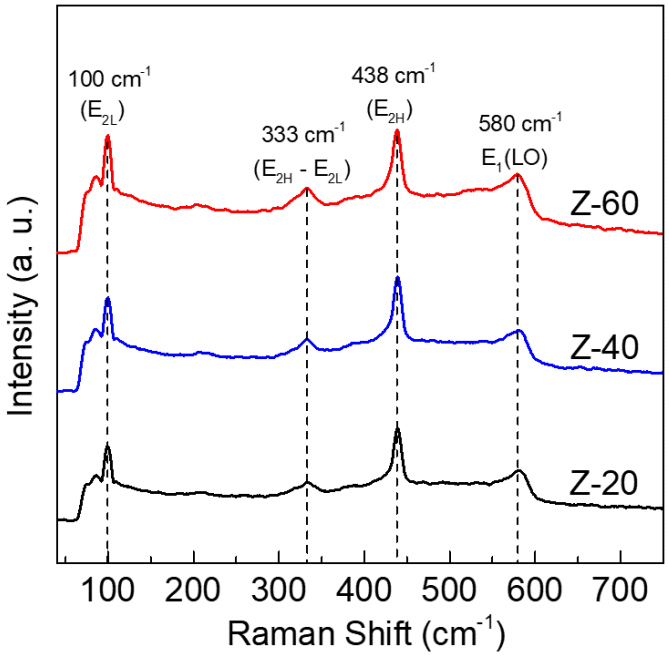

Figure 3. Raman spectra of screen-printed ZnO thick films.

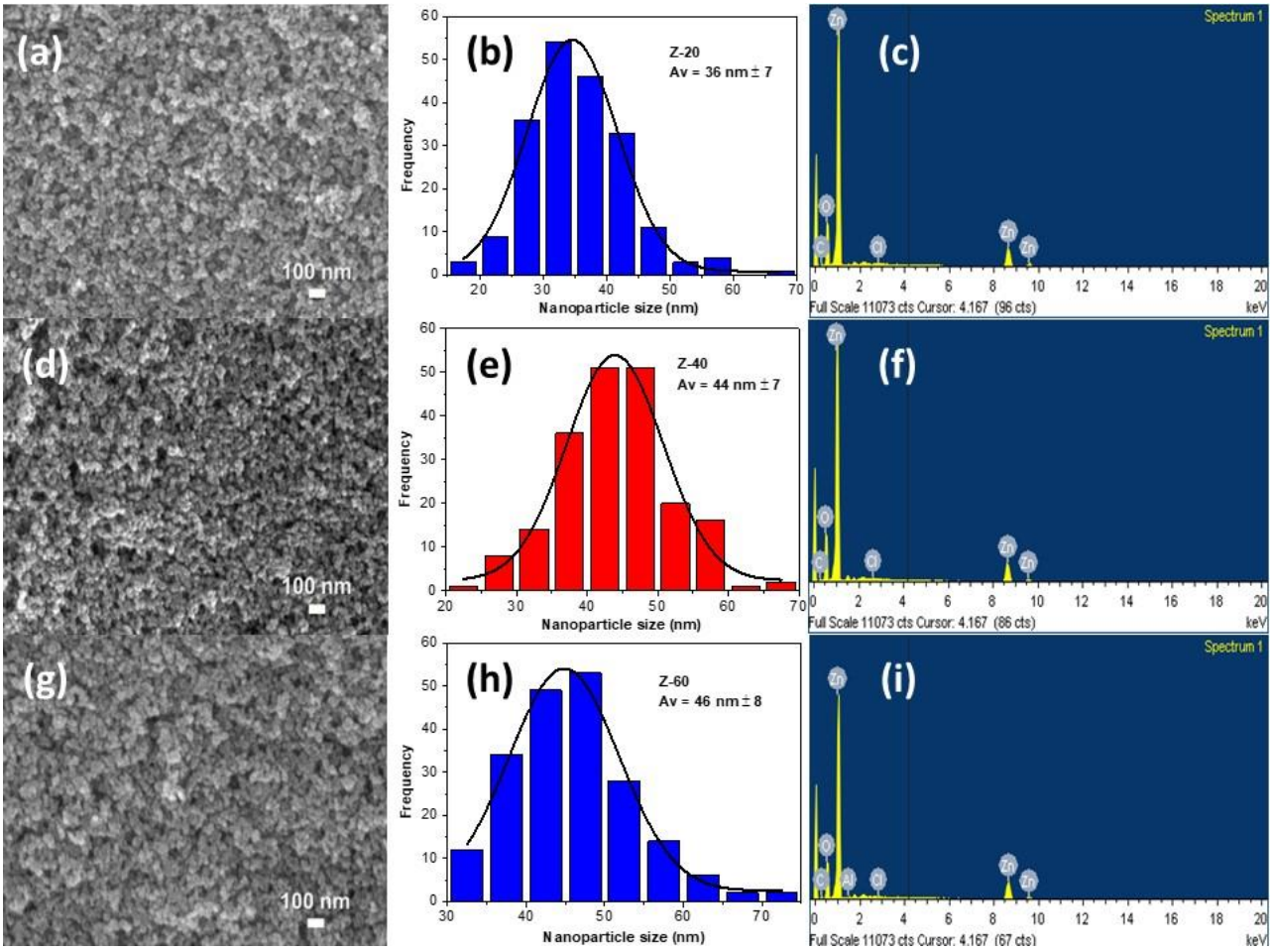

Figure 4. SEM images, size distribution and EDS spectra of the ZnO thick films prepared with ZnO powders at different milling times. (**a**–**c**) Z-20; (**d**–**f**) Z-40; (**g**–**i**) Z-60.

The average thickness of the ZnO thick films was 4.9, 5.2 and 5.4 µm for ZnO thick films Z-20, Z-40 and Z-60, respectively. It was observed that the thickness of the screen printed ZnO thick films measured by profilometry increased with extended milling time as a result of the cycles of deposition and the formation of larger nanoparticles [30]. Additionally, larger crystallites also contributed to the formation of dense thick films, resulting in an increase in thickness [42].

3.4. Surface Analysis of ZnO Thick Films

Figure 5a–f show 2D and 3D images of the surface topography of the ZnO thick films in a scanned area of 10.0 µm × 10.0 µm. The 3D images were processed using the open-source software Gwyddion 2.64, specifically designed for AFM microscopy, data analysis, and visualization [43]. A high-density surface nanostructured with varying sizes is clearly observed in the 2D and 3D images of ZnO thick film, as observed in the SEM micrographs. The roughness results from the root mean square (RMS) of ZnO thick films are 86 ± 10, 88 ± 12, and 85 ± 9 nm for Z-20, Z-40 and Z-60, respectively. In this case, the ZnO thick film with a higher roughness value was Z-40. A high surface roughness is favorable for its application as a gas sensor, since it increases the surface area for interacting with the target gas, enhancing the sensitivity of the ZnO thick film [44,45]. It was observed that for these ZnO thick films, having a lower degree of crystallinity improves their surface roughness; this is because it increases the free energy on the surface, consequently enhancing the roughness [46]. Other factors affecting the roughness of a ZnO thick film include crystal size, nanostructure morphology, substrate and film treatment, film deposition conditions, and precursor solutions concentration [47].

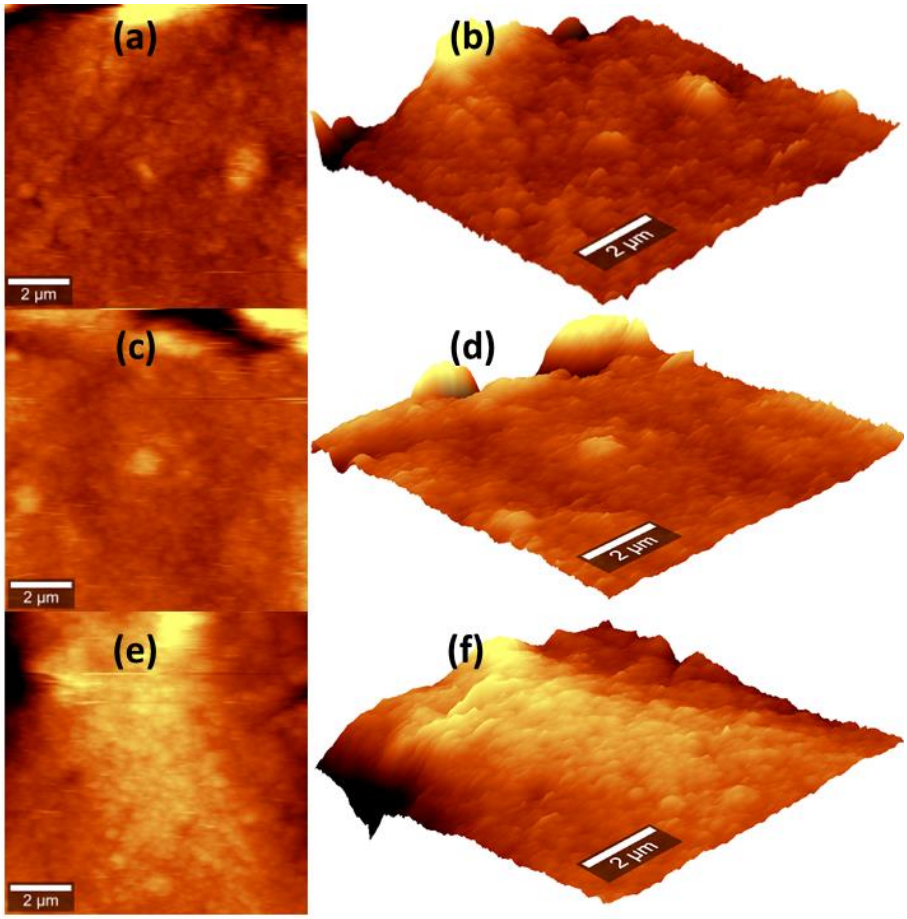

Figure 5. 2D and 3D AFM images of the surface topography of the ZnO thick films. (**a**,**b**) Z-20; (**c**,**d**) Z-40; (**e**,**f**) Z-60.

3.5. Optical Analysis and Electrical Measurement

The optical absorption measurement was conducted for the ZnO thick films in the absorbance mode in the range of 300 to 700 nm. In Figure 6a, absorbance spectrum of ZnO thick films Z-20, Z-40 and Z-60 is presented. The optical spectra of the ZnO thick films shows an absorption peak in the ultraviolet region at approximately 375 nm, which is attributed to the band gap direct transition of the bulk ZnO [48]. It was observed that the absorption intensity in the UV region increased in the ZnO thick films as the synthesis time increased. This increase in absorption intensity is due to all the ZnO thick films having crystallites with preferential growth on the (002) plane, which promotes enhanced absorption in the UV region [49]. The synthesis conditions under which the experiments were conducted did not alter the properties of ZnO to absorb light in the UV region and maintain transparency in the visible region. The optical band gaps were calculated using the Tauc Equation (15) [50]:

$$(\alpha h\nu)^n = A(h\nu - E_g) \quad (15)$$

where α is the absorption coefficient, $h\nu$ is the photon energy, A is a constant, n refers to the type of transition for ZnO, which is a direct band gap semiconductor, n = 2, and E_g is the band gap. For the calculation of the band gap, a linear fit was performed in the straight portion of the curve of $(\alpha h\nu)^2$ against $(h\nu)$. Figure 6b shows the Tauc's plots of the ZnO thick films. The band gap of the ZnO thick films was in the range of 2.77 eV to 3.02 eV. This narrowing of the band gap is attributed to the optical confinement effect due to the dimensions of the ZnO nanoparticles and the thickness of the ZnO thick films, showing a red shift [51]. This behavior was reported when ZnO thick films were manufactured through different deposition cycles, resulting in varying film thicknesses, generating a narrowing of the band gap energy causing a red shift [52]. A similar effect occurs when ZnO is synthesized with high concentrations in the precursor solution, where the absorption edges shifted towards the red, and there was a decrease in the band gap energy [53].

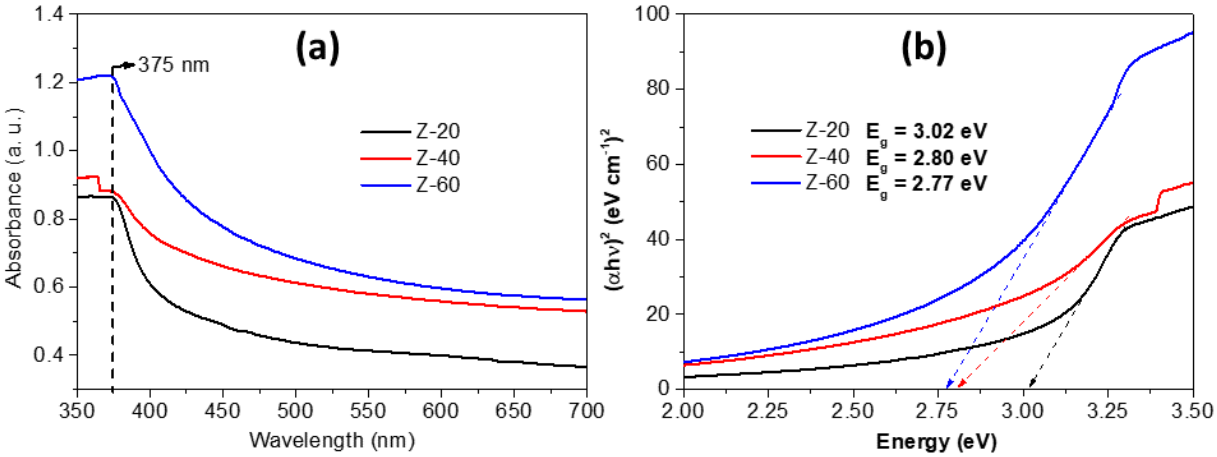

Figure 6. (**a**) Absorbance spectra of ZnO thick films; (**b**) inset Tauc's plots of ZnO thick films.

The electrical measurement of ZnO thick films was performed by using the four-point probe technique. The resistivity was calculated through Equation (16) [54].

$$\rho = \frac{\pi}{\ln 2} * \frac{V}{I} \quad (16)$$

The average resistivity values obtained for the ZnO thick films Z-20, Z-40, and Z-60 were 2.46×10^5 ohm-m, 7.93×10^4 ohm-m, 7.88×10^4 ohm-m, respectively. The resistivity values found for the ZnO thick films were within the range of values reported in the literature for ZnO [55,56]. The decrease in resistivity among the Z-20, Z-40, and Z-60 thick films was related to the milling time used in the fabrication of ZnO, as the Z-60 thick films with 60 min of milling had the lowest resistivity value. This behavior of the Z-60

film is attributed to the larger crystallite size, and it had the lowest value of dislocation density lines compared to the other thick films. These characteristics help to reduce the grain boundaries and promote an increase in carriers concentration [57]. Additionally, the increase in the thickness of the ZnO thick films also contributes to the decrease in resistivity [58].

3.6. Adherence Test of ZnO Thick Films

The ZnO thick films deposited by screen printing on the glass substrate were uniform. The strength of adhesion of ZnO thick films was measured using a Cross Cut Tape Test. The test was conducted in accordance with the ASTM D3359-22 Standard (Standard Test Methods for Measuring Adhesion by Tape Test) [27]. The adhesion of the ZnO thick films was assessed using an adhesive tape by inspecting the film grid for any evidence of removed sections. The ASTM standard has six classifications for adhesion test, indicating the percentage of film detachment from the substrate: Level 5B (0%), 4B (5%), 3B (5%–15%), 2B (15%–35%), 1B (35%–65%), and 0B (>65%). After the ZnO thick films Z-20, Z-40 and Z-60 were tested, it was observed that thick films were still adhered to the substrate with no visible disarray. Figure 7a shows ZnO thick films assessed and compared with scale and designated as '4B' of ASTM classification; this means that 95% of screen-printed material remained due to the strength of adhesion to the glass substrate. The area of ZnO thick film was 10 mm × 10 mm, as shown in Figure 7b. The cross-cut pattern of ZnO screen-printed thick films after the tape test is shown in Figure 7c–e.

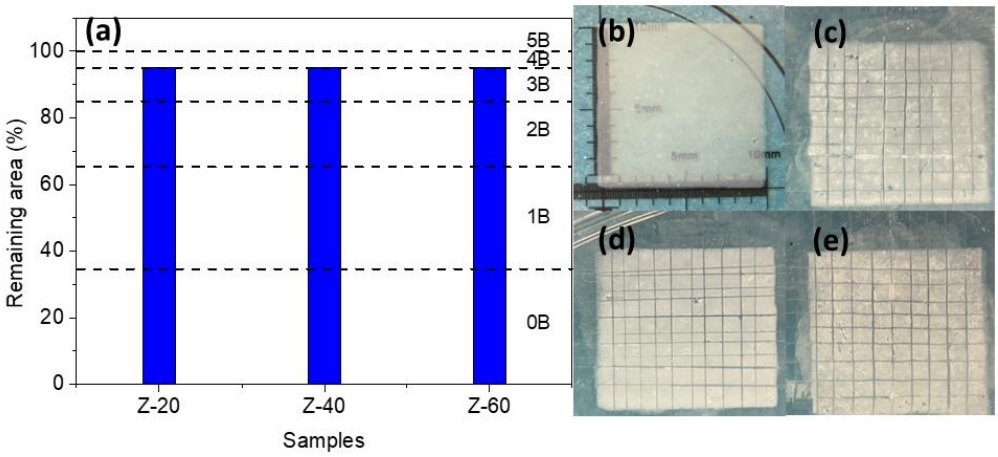

Figure 7. Adherence tests of ZnO thick films based on the ASTM D3359-22. (**a**) ASTM Classification of Adhesion Test of ZnO thick films; (**b**) ZnO thick film area 10 mm × 10 mm before cross cut test. Photographical images of ZnO thick films after tape test: (**c**) Z-20; (**d**) Z-40; (**e**) Z-60.

This test revealed the adhesion strength of the ZnO thick films prepared in this work. These results are similar to those reported for ZnO thick films deposited on glass, where the annealing step enhances the film adhesion on the substrates, considering the temperature of annealing in the range of 400 to 550 °C [19,59].

Adhesion tests were carried out after 12 months of aging and it was found that the aged films exhibited an ASTM classification of 3B (5%–15% detachment). Although it decreased in the ASTM classification, it confirms that the ZnO films manufactured in this work are stable and durable. It can be assumed that the change in adherence is due to excess of moisture on the surface of the film.

3.7. Discussion of Characterization Results

In this work, the main objective was the fabrication of ZnO thick films for their application as an H_2S gas sensor. Once the thick films were fabricated, the next step was to determine the crystalline structure of ZnO through X-ray diffraction, which confirmed the hexagonal wurtzite crystalline structure of ZnO. Furthermore, the XRD data allowed

for the calculation of the crystallite size, which falls within the range of 32–35 nm. This parameter is related to sensor performance, as a smaller size leads to increased sensitivity of the sensor. Another calculated parameter was the texture coefficient, which indicated a preferential growth of ZnO nanostructures on the (002) plane along the c-axis. For a gas sensor, it is desirable for this alignment to occur along the c-axis, as it enhances electron flow during the gas sensing process. Vibrational analysis through Raman spectroscopy confirmed the crystalline structure of ZnO.

Morphological analysis by scanning electron microscopy found a well-defined morphology of nanograins, which were observed to cluster together to form agglomerates, with nanograin sizes ranging from 36 to 46 nm. These nanograins have a high surface-to-volume ratio due to their nanoscale size, facilitating gas molecule adsorption on their surface. The analysis of surface topography by atomic force microscopy allowed the roughness measurement of the ZnO thick films, which was found in the range of 85–88 nm. This indicates that a high roughness value corresponds to a large surface area for interacting with H2S gas, improving the sensitivity. The energy bandgap of ZnO was calculated, and a narrowing in the range of 3.02–2.77 eV was found, attributed to the thickness of the films, confirming its absorption band in the UV region.

The measurement of resistivity of the thick ZnO films using the four-point probe test helped calculate the resistivity values in a range of 7.88×10^4–2.46×10^5 ohm-m. This value is important because lower resistivity reduces the grain boundary and results in a higher flow of charge carriers. Finally, the adhesion tests allowed identification of the strength of film adhesion with the glass substrate, which in this case was 4B for all samples, implying a maximum detachment of 5%. This is beneficial as it indicates that the films can withstand a large number of sensing cycles. All these characterizations helped identify the characteristics of the ZnO films, enabling their application as a gas sensor, as well as comparing the effect of mechanical treatment on milling time and gas sensing efficiency.

3.8. H_2S Gas Sensing Performance

The sensitivity of ZnO sensors manufactured through the mechanochemical method and the screen-printing technique was evaluated in terms of changes in electrical resistance when exposed to H_2S gas, considering concentrations from 25 to 600 ppm, at different low operating temperature ranges from 35 to 80 °C, under continuous UV-LED illumination to assist in the activation of the surface of ZnO. In these H_2S gas sensing tests, humidity control was not conducted. The response time is defined as the required time to reach 90% of total change in electrical resistance upon exposure to target gas, and recovery time is defined as the time taken to reach 10% of total change in electrical resistance in the presence of air. Figure 8a,c,e show the dynamic response curves in percentage of the three sensors Z-20, Z-40, and Z-60, respectively, once exposed to H_2S gas concentrations at different low operating temperatures under continuous UV-LED illumination. It can be observed that the response of ZnO sensors increases proportionally as the concentrations of the H_2S gas increase. The highest response value was 22.40%, obtained in the test for 600 ppm of H_2S gas at 65 °C with the Z-40 sensor. On the other hand, the lowest response value was 3.93%, observed in the test for 25 ppm of H_2S gas at 35 °C with the Z-60 sensor. It is noteworthy that the highest response values were obtained at 65 °C. In these tests under continuous UV-LED illumination, the sensor that experienced a greater effect was the Z-40. This effect promoted higher sensitivity, yielding the highest response values across different concentrations and low operating temperatures. This sensor was synthesized with a milling time of 40 min, and the Z-40 sensor exhibited the highest roughness, which helps to provide a larger surface to be in contact with the H_2S gas. Other characteristics contributing to this high sensitivity of the Z-40 sensor include the small size of the crystallite, since in the literature we can find that for higher sensitivity, D should have values less than 30 nm [60]. It has been reported that a thinner sensor film and smaller crystal size help to increase sensitivity of the sensor as the grain boundary enlarges [61]. The growth aligned with the C-axis helps electron transfer between the gas molecules and the surface

of the ZnO sensor [38]. The response and recovery cycles of ZnO sensors that occurred at different low operating temperatures under continuous UV-LED illumination are presented in Figure 8b,d,f. During H_2S gas sensing tests, electrical resistance was measured. The Z-20, Z-40, and Z-60 sensors exhibit good reproducibility in sensing tests, as well as good reversibility toward different concentrations of the H_2S gas.

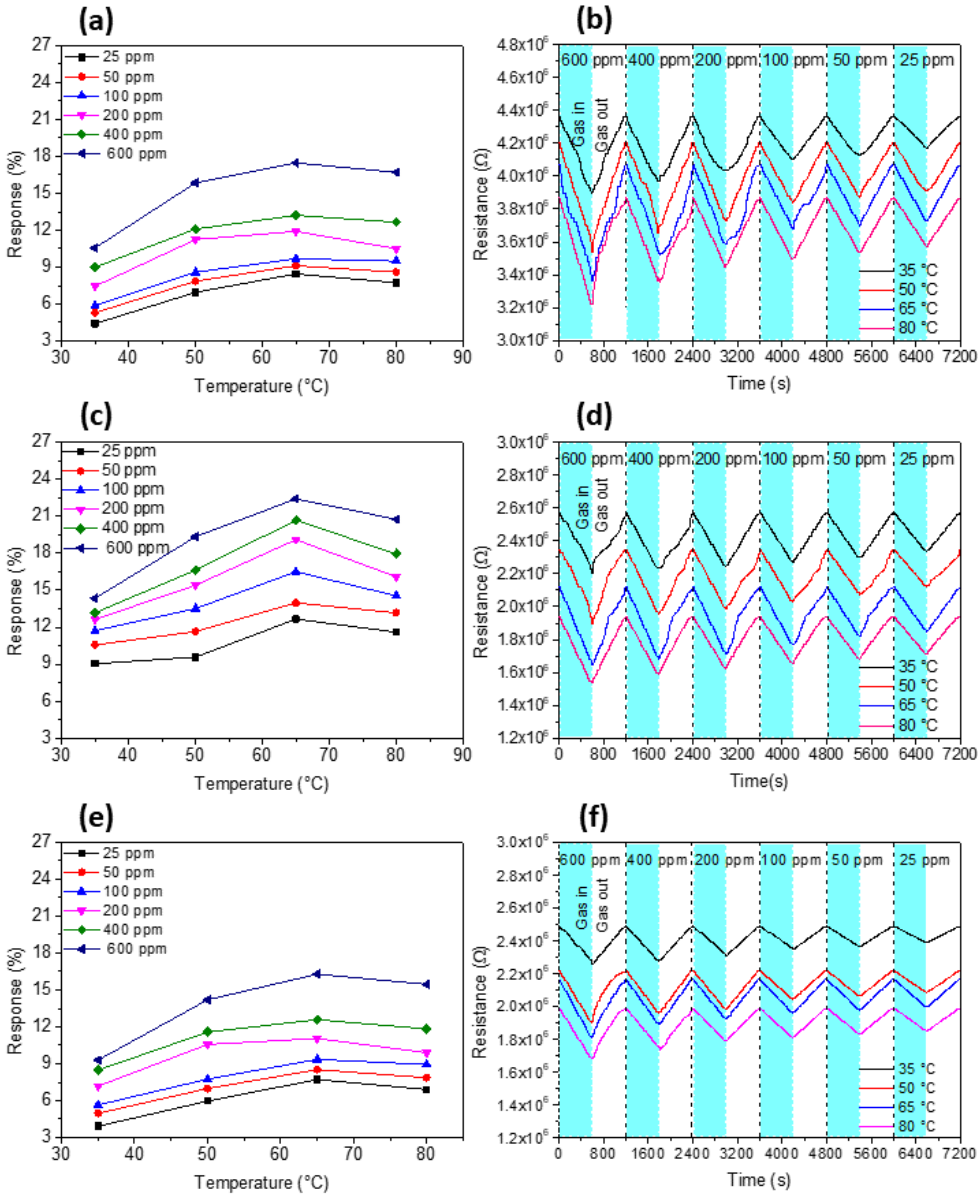

Figure 8. Dynamic response curves of the ZnO sensors toward 25, 50, 100, 200, 400, and 600 ppm of H_2S gas at low temperatures from 35 to 80 °C under continuous UV-LED illumination. Response curves in percentage: (**a**) Z-20; (**c**) Z-40; (**e**) Z-60, and response curves based on electrical resistance: (**b**) Z-20; (**d**) Z-40; (**f**) Z-60.

The effect of continuous UV-LED illumination on the sensitivity of the ZnO sensor to H_2S gas was evaluated. As an example, the performance of the Z-40 sensor, which achieved the best results in previous tests, is presented in Figure 9a–f. In these sensing tests, concentrations ranging from 25 to 600 ppm of H_2S gas and low operating temperatures in the range of 35 to 80 °C were considered, both without continuous UV-LED illumination and with continuous UV-LED illumination. It can be observed that the tests showed detectable responses even without continuous UV-LED illumination. The response values ranged from 9.05 to 22.40% for the tests with continuous UV-LED illumination, while for

without continuous UV-LED illumination, the response ranged from 4.98 to 17.5%. The influence of continuous UV-LED illumination was remarkable from 35 to 65 °C, highlighted in Figure 9a–f. The data presented in Figure 9a–f show that the sensitivity of Z-40 sensor was enhanced by continuous UV-LED illumination compared to the tests that did not have its assistance. The response increased up to 116% in the sensing test for 600 ppm of H_2S gas at 65 °C. As observed in Figure 9, it had the highest values in these tests. This behavior of the ZnO sensor is related to its two polar faces—one terminated with Zn^{2+} (positive) and the other with O^{2-} (negative)—due to the electric field generated by these two surfaces. When the ZnO nanoparticles receive continuous UV-LED illumination, the photoinduced electrons prefer to migrate and accumulate on the positive polar face (002) and the photoinduced holes on the non-polar face (100) [62]. Continuous UV-LED illumination increases the conductivity and sensitivity of the ZnO sensor even at room temperature. This is because UV light with energy comparable to the band gap of ZnO is capable of accelerating the absorption and desorption process of gas molecules on the surface of ZnO due to the generation of photogenerated electron-hole pairs, assisting the ZnO sensor at low operating temperatures such as room temperature. On the other hand, when the low operating temperature reaches 80 °C, the sensitivity of the ZnO sensor is almost independent of continuous UV-LED illumination. At this point, thermal energy has the greatest effect on the surface of ZnO, helping to increase the density of charge carriers and the exchange of electrons between the H_2S gas molecules and the surface of ZnO.

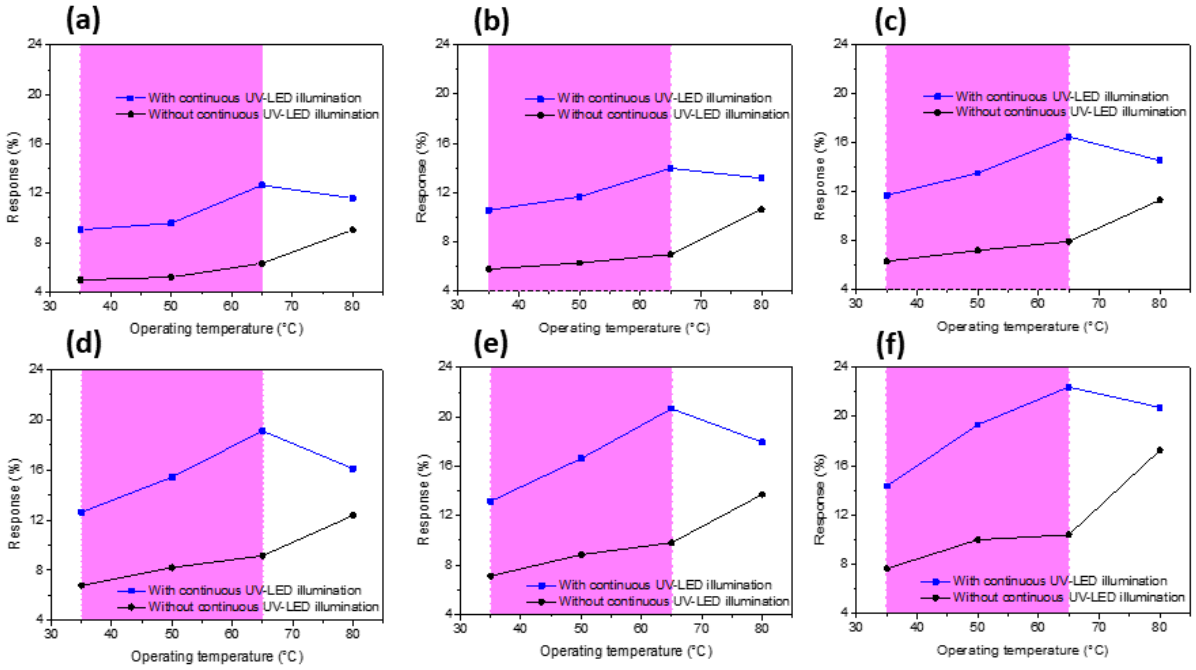

Figure 9. The temperature dependence of response to H_2S gas of the Z-40 sensor at temperatures from 35 to 80 °C under continuous UV-LED illumination. (**a**) 25 ppm; (**b**) 50 ppm; (**c**) 100 ppm; (**d**) 200 ppm; (**e**) 400 ppm; (**f**) 600 ppm.

In Figure 10a, the results of the selectivity tests conducted with the Z-40 sensor are shown. The Z-40 sensor was tested with five gases: C_3H_8O, C_2H_6O, C_3H_6O, LPG, and H_2S. The test conditions were 600 ppm of each gas at low operating temperatures of 65 °C under continuous UV-LED illumination, and humidity control was not performed. In the results, a higher selectivity for the H_2S gas is observed, with an average of 40% more than the other gases. The selectivity of the ZnO sensor towards H_2S gas is related to the small molecular size of H_2S gas compared to the other gases tested, and this characteristic is beneficial in the detection of H_2S gas as it allows for a greater number of molecules to be absorbed on the surface of ZnO [63]. Other measurements conducted with the ZnO sensors included long-term stability, shown in Figure 10b. A test was conducted once a

week for 12 weeks considering the conditions of tests at 65 °C with 600 ppm of H_2S gas. The ZnO sensors fabricated in this work exhibited good stability after 12 weeks, with an average decrease of 2.5% in the response. This is due to the stability of the hexagonal wurtzite crystalline structure of ZnO, as well as the fact that the film demonstrated strong adhesion to the substrate. In Figure 10c, the comparison of response time and recovery time for the Z-40 sensor is presented. The test was carried out with 600 ppm of H_2S gas at 65 °C, both with and without continuous UV-LED illumination. For the response time and recovery time, a difference of ca. 60 s was observed when utilizing continuous UV-LED illumination. On average, the response time for sensing tests was 518 s, and the recovery time was 543 s. With all the aforementioned results, it was demonstrated that the ZnO thick films manufactured in this work can be used for the detection of H_2S gas.

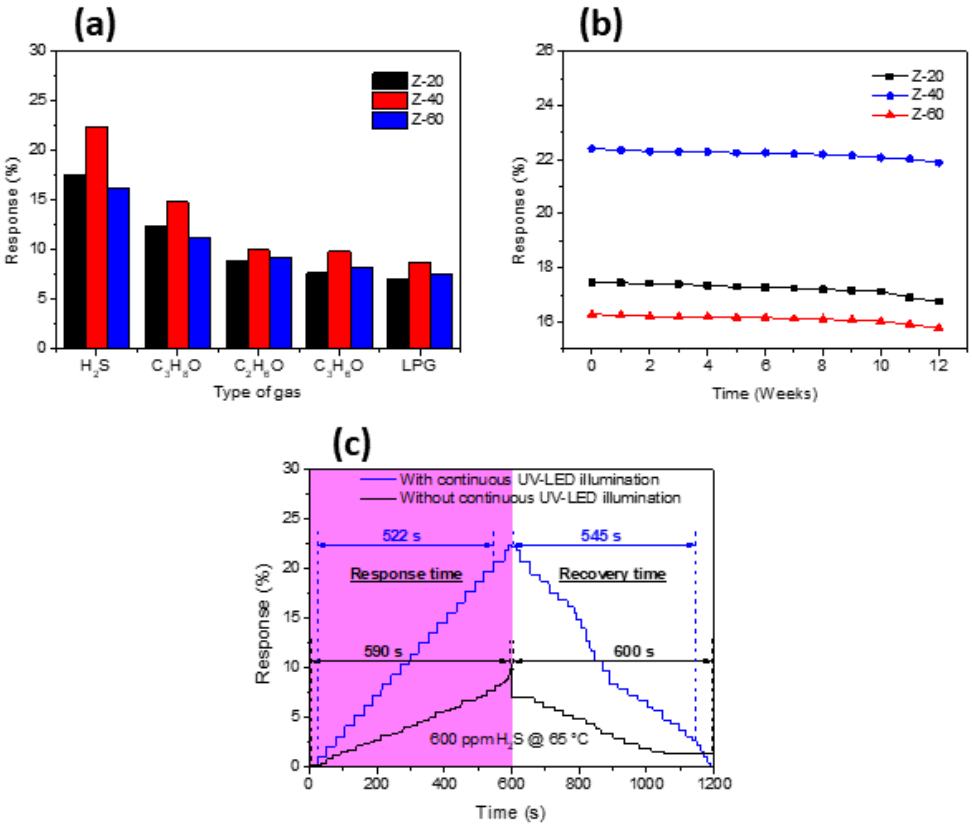

Figure 10. (**a**) Selectivity test of Z-20/Z-40/Z-60 sensors toward 600 ppm of different gases at 65 °C under continuous UV-LED illumination; (**b**) long-term stability test of Z-20/Z-40/Z-60 sensors toward 600 ppm of H_2S gas at 65 °C under continuous UV-LED illumination; (**c**) response and recovery time of Z-40 sensor.

3.9. Sensing Mechanism of ZnO Sensor

The sketch of the sensing mechanism of the ZnO sensor is presented in Figure 11. The sensing mechanism of the ZnO sensor is based on the adsorption and desorption of molecules on its surface. This process begins when the ZnO sensor is exposed to air, where the chemisorption of oxygen (O_2) takes place. This can occur at room temperature and at high temperatures (100–500 °C). The O_2 molecules can be ionosorbed in molecular (O_2^-) or atomic form (O^- and O^{2-}), and this occurs with the transfer of electrons between the surface of the ZnO and the surrounding O_2 ions. At temperatures below 100 °C, the adsorbed oxygen is in the form of O_2^-. In this case, the ZnO sensor is under continuous UV-LED illumination, where generation of photogenerated electron–hole pairs occurs;

then, oxygen molecules trap photogenerated electrons from the conduction band of ZnO, forming negative species [64]. This is shown in the following equation:

$$O_{2(gas)} + e^-_{(h\upsilon)} \rightarrow O^-_{2(h\upsilon)} \quad (17)$$

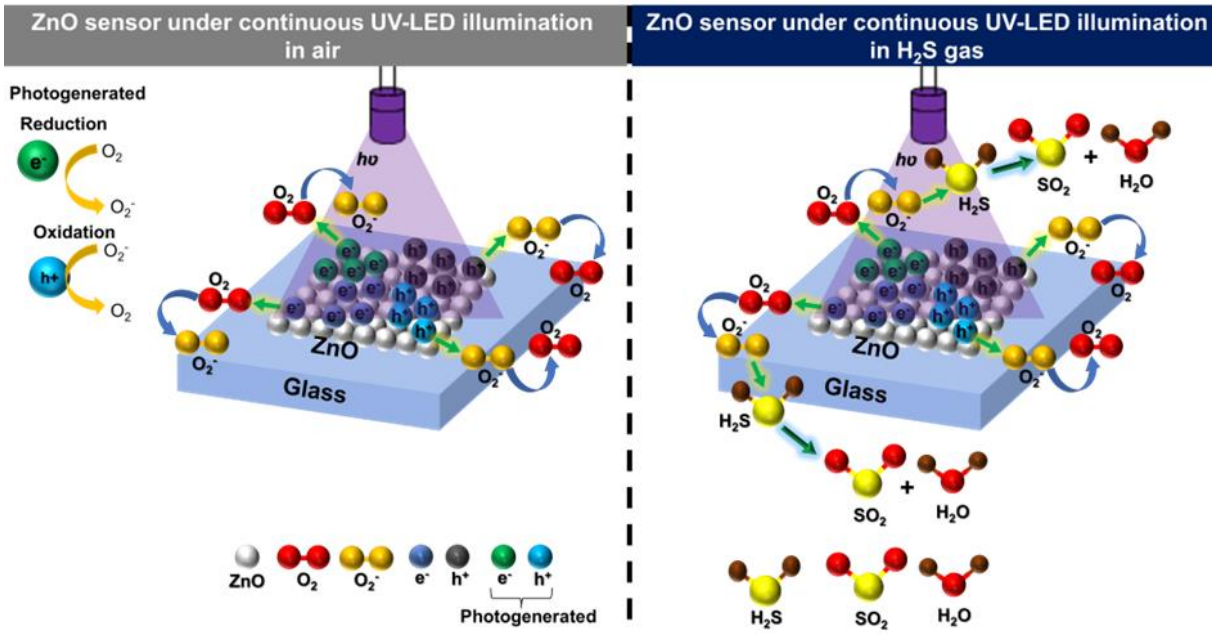

Figure 11. Sketch of the sensing mechanism of the ZnO sensor exposed to air and H_2S gas.

This process results in the formation of an electron depletion layer (EDL) with a decrease in the density of carrier charge and with an increase in electrical resistance of the ZnO sensor. On the other hand, when the ZnO sensor is exposed to H_2S gas molecules, these are absorbed on the surface of ZnO, and they will react with the chemisorbed oxygen ions. These chemical reactions promote the release of electrons, which return to the EDL. With this, a reduction of the potential barrier energy occurs. As a result, the electrical resistance on the surface of ZnO is decreased. This interaction is described with the following equation:

$$2H_2S + 3O^-_{2(h\upsilon)} \rightarrow 2SO_2 + 2H_2O + 6e^- \quad (18)$$

It is well known that UV illumination generates a large number of photogenerated electrons and holes (pairs) on the surface of ZnO because the photon energy is higher than the bandgap energy. Then, the photogenerated holes interact with oxygen species on the surface of the ZnO sensor, leading to the desorption of oxygen molecules and a decrease in the EDL. This is observed in the following equation [65].

$$h^+_{(h\upsilon)} + O^-_{2(ads)} \rightarrow O_{2(g)} \quad (19)$$

In Table 4, a comparison of the results of H_2S gas sensing of UV-assisted ZnO sensors published in recent years and those obtained in this work is presented. From the published works, it was observed that they detect H_2S gas concentrations between 1 and 1000 ppm and operate at room temperature. They exhibited a detectable response. Therefore, the operating temperature, response and tested concentrations of gas with the sensors in this work are satisfactory.

Table 4. ZnO gas sensors assisted with UV light.

Sensing Material	Gas Concentration	Operating Temperature (°C)	Sensor Response	Ref.
Au-ZnO	H_2S (5 ppm)	RT	1.01 (Ra/Rg)	[66]
In_2O_3/ZnO	H_2S (1 ppm)	RT	1.30 (Ra/Rg)	[67]
Au-ZnO	H_2S (1000 ppm)	250	18.12% ((Ra/Rg − 1)·100%)	[68]
ZnO	H_2S (5 ppm)	RT	10.24% ((Ra − Rg/Ra)·100%)	[69]
Co-ZnO	H_2S (100 ppm)	RT	2.50 (Ig/Ia)	[70]
ZnO	H_2S (100 ppm)	RT	1.08 (Ra/Rg)	[71]
ZnO	H_2S (100 ppm)	RT	6.8 (Ra/Rg)	[72]
ZnO	H_2S (25 ppm)	65	12.66% ((Ra − Rg/Ra)·100%)	This work
ZnO	H_2S (100 ppm)	65	16.50% ((Ra − Rg/Ra)·100%)	This work
ZnO	H_2S (600 ppm)	65	26.40% ((Ra − Rg/Ra)·100%)	This work

4. Conclusions

ZnO nanostructures were successfully prepared applying a sequential mechanochemical and screen-printing methodology. These results show that it is possible to obtain high quality coatings after 20–40 min of grinding, without affecting the final characteristics of the film. The results of the diffraction patterns show that for all the synthesized systems, the wurtzite-type hexagonal phase stabilized, without detecting the presence of residual oxides. The synthesis process, presented in this work, is a very simple manufacturing process with relatively low temperatures with high reproducibility, capable of promoting the formation of a stable film for producing large quantities of gas-sensing films. The sensing response of ZnO film sensor (Z-40) to 600 ppm of H_2S gas at the low operating temperature of 65 °C was increased up to 116% under continuous UV-LED illumination activation. Under continuous UV-LED illumination, the ZnO sensor exhibited faster response/recovery times than without continuous UV-LED illumination and better selectivity for the same H_2S concentration. These results suggest that the combination of continuous UV-LED illumination and low operating temperature had a synergistic effect that helped to increase the sensitivity of the ZnO sensor with low energy consumption. The significant increase in the sensing response of ZnO sensor under continuous UV-LED illumination might be due to the rise in charge carriers caused by the photogenerated electron–hole pairs, which promote an important change in the values of electrical resistance upon exposure to H_2S gas molecules. These results should be considered when developing metal oxide gas sensors activated by UV or visible light with low energy consumption for monitoring toxic gases. These metal oxide gas sensors can also be extended on flexible substrates.

Author Contributions: Conceptualization, C.M.-P., J.L.C.-L. and L.L.D.-F.; methodology, C.M.-P., A.d.R.L.-G. and L.L.D.-F.; experimental process, C.M.-P.; formal analysis, C.M.-P., J.L.C.-L., A.d.R.L.-G., A.S.L.-R., P.S.-G., J.C.D.-G. and L.L.D.-F.; writing—original draft preparation, C.M.-P.; writing—review and editing, C.M.-P., J.L.C.-L., A.d.R.L.-G., A.S.L.-R., P.S.-G., J.C.D.-G. and L.L.D.-F.; supervision, L.L.D.-F. All authors have read and agreed to the published version of the manuscript.

Funding: C. Martínez-Pacheco thanks the support of the scholarship CONAHCYT with number 946800. J. L. Cervantes-López acknowledges the support of the scholarship PRODEP with part number SSA-542319.

Institutional Review Board Statement: Not applicable.

Informed Consent Statement: Not applicable.

Data Availability Statement: All data are included in the manuscript.

Acknowledgments: The authors appreciate the support provided by Patricia Quintana during her stay in the laboratory LANNBIO. In addition, the authors thank the technical help provided by the technical staff of Cinvestav-Unidad Mérida, in particular Dora A. Huerta, Montserrat Soria and Víctor Rejón (SEM), José Bante (Raman and AFM) and Daniel Aguilar Treviño (XRD).

Conflicts of Interest: The authors declare no conflicts of interest.

References

1. Sha, R.; Basak, A.; Maity, P.C.; Badhulika, S. ZnO Nano-Structured Based Devices for Chemical and Optical Sensing Applications. *Sens. Actuators Rep.* **2022**, *4*, 100098. [CrossRef]
2. Viter, R.; Iatsunskyi, I. Metal Oxide Nanostructures in Sensing. In *Nanomaterials Design for Sensing Applications*; Zenkina, O.V., Ed.; Elsevier: Amsterdam, The Netherlands, 2019; pp. 41–91. [CrossRef]
3. Sambasevam, K.P.; Sateria, S.F.; Baharin, S.N.A.; Azman, N.J.; Ahmad Wakid, S.; Shahabuddin, S. An Optimization of Fungal Chitin Grafted Polyaniline for Ammonia Gas Detection via Box Behnken Design. *Int. J. Biol. Macromol.* **2023**, *238*, 124079. [CrossRef] [PubMed]
4. Qi, B.; Wang, X.; Wang, X.; Cheng, J.; Shang, Y. Synthesis and H_2S-Sensing Properties of MOF-Derived Cu-Doped ZnO Nanocages. *Nanomaterials* **2022**, *12*, 2579. [CrossRef] [PubMed]
5. Mahajan, S.; Jagtap, S. Nanomaterials-Based Resistive Sensors for Detection of Environmentally Hazardous H_2S Gas. *J. Electron. Mater.* **2021**, *50*, 2531–2555. [CrossRef]
6. Nagarjuna, Y.; Lin, J.-C.; Wang, S.-C.; Hsiao, W.-T.; Hsiao, Y.-J. AZO-Based ZnO Nanosheet MEMS Sensor with Different Al Concentrations for Enhanced H_2S Gas Sensing. *Nanomaterials* **2021**, *11*, 3377. [CrossRef] [PubMed]
7. Li, T.; Yin, W.; Gao, S.; Sun, Y.; Xu, P.; Wu, S.; Kong, H.; Yang, G.; Wei, G. The Combination of Two-Dimensional Nanomaterials with Metal Oxide Nanoparticles for Gas Sensors: A Review. *Nanomaterials* **2022**, *12*, 982. [CrossRef] [PubMed]
8. Yoon, Y.; Truong, P.L.; Lee, D.; Ko, S.H. Metal-Oxide Nanomaterials Synthesis and Applications in Flexible and Wearable Sensors. *ACS Nanosci. Au* **2022**, *2*, 64–92. [CrossRef] [PubMed]
9. Crispi, S.; Neri, G. Development of a Conductometric Sensor Based on Al,Ca-Doped ZnO for the Detection of Formaldehyde. *Sensors* **2022**, *22*, 7465. [CrossRef] [PubMed]
10. Habibi, A.; Vatandoust, L.; Aref, S.M.; Naghshara, H. Formation of High Performance Nanostructured ZnO Thin Films as a Function of Annealing Temperature: Structural and Optical Properties. *Surf. Interfaces* **2020**, *21*, 100723. [CrossRef]
11. Wang, C.N.; Li, Y.L.; Gong, F.L.; Zhang, Y.H.; Fang, S.M.; Zhang, H.L. Advances in Doped ZnO Nanostructures for Gas Sensor. *Chem. Rec.* **2020**, *20*, 1553–1567. [CrossRef] [PubMed]
12. Platonov, V.; Malinin, N.; Vasiliev, R.; Rumyantseva, M. Room Temperature UV-Activated NO_2 and NO Detection by ZnO/RGO Composites. *Chemosensors* **2023**, *11*, 227. [CrossRef]
13. Kisan, B.; Kumar, J.; Alagarsamy, P. Experimental and First-Principles Study of Defect-Induced Electronic and Magnetic Properties of ZnO Nanocrystals. *J. Phys. Chem. Solids* **2020**, *146*, 109580. [CrossRef]
14. Prete, P.; Lovergine, N.; Tapfer, L. Nanostructure Size Evolution during Au-Catalysed Growth by Carbo-Thermal Evaporation of Well-Aligned ZnO Nanowires on (100)Si. *Appl. Phys. A* **2007**, *88*, 21–26. [CrossRef]
15. Reddy, I.N.; Reddy, C.V.; Sreedhar, M.; Cho, M.; Shim, J.; Reddy, V.R.; Choi, C.-J.; Kim, D. Effect of Seed Layers (Al, Ti) on Optical and Morphology of Fe-Doped ZnO Thin Film Nanowires Grown on Si Substrate via Electron Beam Evaporation. *Mater. Sci. Semicond. Process.* **2017**, *71*, 296–303. [CrossRef]
16. Singh, J.; Sharma, S.; Soni, S.; Sharma, S.; Chand Singh, R. Influence of Different Milling Media on Structural, Morphological and Optical Properties of the ZnO Nanoparticles Synthesized by Ball Milling Process. *Mater. Sci. Semicond. Process.* **2019**, *98*, 29–38. [CrossRef]
17. Jamkhande, P.G.; Ghule, N.W.; Bamer, A.H.; Kalaskar, M.G. Metal Nanoparticles Synthesis: An Overview on Methods of Preparation, Advantages and Disadvantages, and Applications. *J. Drug Deliv. Sci. Technol.* **2019**, *53*, 101174. [CrossRef]
18. Sapkota, R.; Duan, P.; Kumar, T.; Venkataraman, A.; Papadopoulos, C. Thin Film Gas Sensors Based on Planetary Ball-Milled Zinc Oxide Nanoinks: Effect of Milling Parameters on Sensing Performance. *Appl. Sci.* **2021**, *11*, 9676. [CrossRef]
19. Manjunath, G.; Pujari, S.; Patil, D.R.; Mandal, S. A Scalable Screen-Printed High Performance ZnO-UV and Gas Sensor: Effect of Solution Combustion. *Mater. Sci. Semicond. Process.* **2020**, *107*, 104828. [CrossRef]
20. Sankapal, B.R.; Gupta, R.B.; Ennaoui, A.; Lokhande, C.D. *Simple Chemical Methods for Thin Film Deposition*; Sankapal, B.R., Gupta, R.B., Ennaoui, A., Lokhande, C.D., Eds.; Springer: Gateway East, Singapore, 2023.
21. Sopiha, K.V.; Kim, J.H.; Kim, S.S.; Wu, P. Gas Sensing Properties of Standard Soda-Lime Glass. *Sens. Actuators B Chem.* **2018**, *266*, 344–353. [CrossRef]
22. Ahmadpour, G.; Nilforoushan, M.R.; Shayegh Boroujeny, B.; Tayebi, M.; Jesmani, S.M. Effect of Substrate Surface Treatment on the Hydrothermal Synthesis of Zinc Oxide Nanostructures. *Ceram. Int.* **2022**, *48*, 2323–2329. [CrossRef]
23. Solomatin, M.A.; Glukhova, O.E.; Fedorov, F.S.; Sommer, M.; Shunaev, V.V.; Varezhnikov, A.S.; Nasibulin, A.G.; Ushakov, N.M.; Sysoev, V.V. The UV Effect on the Chemiresistive Response of ZnO Nanostructures to Isopropanol and Benzene at PPM Concentrations in Mixture with Dry and Wet Air. *Chemosensors* **2021**, *9*, 181. [CrossRef]
24. Li, T.; Xu, L.; Wang, Y. Micro-Heater-Based Gas Sensors—Micro Electro Mechanical Systems. In *Micro Electro Mechanical Systems*; Huang, Q.-A., Ed.; Springer: Singapore, 2017; pp. 1–37. [CrossRef]
25. Franco, M.A.; Conti, P.P.; Andre, R.S.; Correa, D.S. A Review on Chemiresistive ZnO Gas Sensors. *Sens. Actuators Rep.* **2022**, *4*, 100100. [CrossRef]
26. Nikolic, M.V.; Milovanovic, V.; Vasiljevic, Z.Z.; Stamenkovic, Z. Semiconductor Gas Sensors: Materials, Technology, Design, and Application. *Sensors* **2020**, *20*, 6694. [CrossRef] [PubMed]

27. *ASTM D3359-22*; Standard Test Methods for Rating Adhesion by Tape. American Society for Testing and Materials: West Conshohocken, PA, USA, 2022.
28. Diao, K.; Zhou, M.; Zhang, J.; Tang, Y.; Wang, S.; Cui, X. High Response to H_2S Gas with Facile Synthesized Hierarchical ZnO Microstructures. *Sens. Actuators B Chem.* **2015**, *219*, 30–37. [CrossRef]
29. Hsu, K.C.; Fang, T.H.; Hsiao, Y.J.; Li, Z.J. Rapid Detection of Low Concentrations of H_2S Using CuO-Doped ZnO Nanofibers. *J. Alloys Compd.* **2021**, *852*, 157014. [CrossRef]
30. Manikandan, B.; Endo, T.; Kaneko, S.; Murali, K.R.; John, R. Properties of Sol Gel Synthesized ZnO Nanoparticles. *J. Mater. Sci. Mater. Electron.* **2018**, *29*, 9474–9485. [CrossRef]
31. Kathwate, L.H.; Umadevi, G.; Kulal, P.M.; Nagaraju, P.; Dubal, D.P.; Nanjundan, A.K.; Mote, V.D. Ammonia Gas Sensing Properties of Al Doped ZnO Thin Films. *Sens. Actuators A Phys.* **2020**, *313*, 112193. [CrossRef]
32. Narayanan, N.; Deepak, N.K. Impact of N Doping on the Physical Properties of ZnO Thin Films. *Surf. Rev. Lett.* **2018**, *25*, 1850035. [CrossRef]
33. Yousefi, H.R.; Hashemi, B.; Mirzaei, A.; Roshan, H.; Sheikhi, M.H. Effect of Ag on the ZnO Nanoparticles Properties as an Ethanol Vapor Sensor. *Mater. Sci. Semicond. Process.* **2020**, *117*, 105172. [CrossRef]
34. Srinivasulu, T.; Saritha, K.; Reddy, K.T.R. Synthesis and Characterization of Fe-Doped ZnO Thin Films Deposited by Chemical Spray Pyrolysis. *Mod. Electron. Mater.* **2017**, *3*, 76–85. [CrossRef]
35. Ait Abdelouhab, Z.; Djouadi, D.; Chelouche, A.; Hammiche, L.; Touam, T. Effects of Precursors and Caustic Bases on Structural and Vibrational Properties of ZnO Nanostructures Elaborated by Hydrothermal Method. *Solid State Sci.* **2019**, *89*, 93–99. [CrossRef]
36. Otis, G.; Ejgenberg, M.; Mastai, Y. Solvent-Free Mechanochemical Synthesis of ZnO Nanoparticles by High-Energy Ball Milling of ε-$Zn(OH)_2$ Crystals. *Nanomaterials* **2021**, *11*, 238. [CrossRef] [PubMed]
37. Cervantes-López, J.L.; Rangel, R.; Cedeño, V.J.; Alvarado-Gil, J.J.; Quintana, P.; Contreras, O.; Espino, J. Controlling the Aspect Ratio of Zn(1−x)Eu(x)O Nanostructures Obtained by a Statistical Experimental Design Involving Atomic Layer Deposition and Microwave-Assisted Hydrothermal Methods. *Appl. Phys. A* **2019**, *125*, 41. [CrossRef]
38. Yu, A.; Li, Z.; Yi, J. Selective Detection of Parts-per-Billion H_2S with Pt-Decorated ZnO Nanorods. *Sens. Actuators B Chem.* **2021**, *333*, 129545. [CrossRef]
39. Horzum, S.; Iyikanat, F.; Senger, R.T.; Çelebi, C.; Sbeta, M.; Yildiz, A.; Serin, T. Monitoring the Characteristic Properties of Ga-Doped ZnO by Raman Spectroscopy and Atomic Scale Calculations. *J. Mol. Struct.* **2019**, *1180*, 505–511. [CrossRef]
40. Song, Y.; Zhang, S.; Zhang, C.; Yang, Y.; Lv, K. Raman Spectra and Microstructure of Zinc Oxide Irradiated with Swift Heavy Ion. *Crystals* **2019**, *9*, 395. [CrossRef]
41. Prommalikit, C.; Mekprasart, W.; Pecharapa, W. Effect of Milling Speed and Time on Ultrafine ZnO Powder by High Energy Ball Milling Technique. *J. Phys. Conf. Ser.* **2019**, *1259*, 12023. [CrossRef]
42. Ji, L.-W.; Peng, S.-M.; Wu, J.-S.; Shih, W.-S.; Wu, C.-Z.; Tang, I.-T. Effect of Seed Layer on the Growth of Well-Aligned ZnO Nanowires. *J. Phys. Chem. Solids* **2009**, *70*, 1359–1362. [CrossRef]
43. Kaźmierczak-Bałata, A.; Bodzenta, J.; Guziewicz, M. Microscopic Investigations of Morphology and Thermal Properties of ZnO Thin Films Grown by Atomic Layer Deposition Method. *Ultramicroscopy* **2020**, *210*, 112923. [CrossRef]
44. Kumar, M.; Singh, B.; Yadav, P.; Bhatt, V.; Kumar, M.; Singh, K.; Abhyankar, A.C.; Kumar, A.; Yun, J.-H. Effect of Structural Defects, Surface Roughness on Sensing Properties of Al Doped ZnO Thin Films Deposited by Chemical Spray Pyrolysis Technique. *Ceram. Int.* **2017**, *43*, 3562–3568. [CrossRef]
45. Saad, R.; Gamal, A.; Zayed, M.; Ahmed, A.M.; Shaban, M.; BinSabt, M.; Rabia, M.; Hamdy, H. Fabrication of ZnO/CNTs for Application in CO2 Sensor at Room Temperature. *Nanomaterials* **2021**, *11*, 3087. [CrossRef] [PubMed]
46. Sharma, A.; Khangarot, R.K.; Kumar, N.; Chattopadhyay, S.; Misra, K.P. Rise in UV and Blue Emission and Reduction of Surface Roughness Due to the Presence of Ag and Al in Monocrystalline ZnO Films Grown by Sol-Gel Spin Coating. *Mater. Technol.* **2021**, *36*, 541–551. [CrossRef]
47. Amakali, T.; Daniel, L.S.; Uahengo, V.; Dzade, N.Y.; de Leeuw, N.H. Structural and Optical Properties of ZnO Thin Films Prepared by Molecular Precursor and Sol–Gel Methods. *Crystals* **2020**, *10*, 132. [CrossRef]
48. Filip, A.; Musat, V.; Tigau, N.; Polosan, S.; Pimentel, A.; Ferreira, S.; Gomes, D.; Calmeiro, T.; Martins, R.; Fortunato, E. ZnO Nanostructures Grown on ITO Coated Glass Substrate by Hybrid Microwave-Assisted Hydrothermal Method. *Optik* **2020**, *208*, 164372. [CrossRef]
49. Roza, L.; Fauzia, V.; Rahman, M.Y.A. Tailoring the Active Surface Sites of ZnO Nanorods on the Glass Substrate for Photocatalytic Activity Enhancement. *Surf. Interfaces* **2019**, *15*, 117–124. [CrossRef]
50. Speaks, D.T. Effect of Concentration, Aging, and Annealing on Sol Gel ZnO and Al-Doped ZnO Thin Films. *Int. J. Mech. Mater. Eng.* **2020**, *15*, 2. [CrossRef]
51. Musa, I.; Qamhieh, N.; Mahmoud, S.T. Synthesis and Length Dependent Photoluminescence Property of Zinc Oxide Nanorods. *Results Phys.* **2017**, *7*, 3552–3556. [CrossRef]
52. Soudi, J.; Sandeep, K.M.; Sarojini, B.K.; Patil, P.S.; Maidur, S.R.; Balakrishna, K.M. Thermo-Optic Effects Mediated Self Focusing Mechanism and Optical Power Limiting Studies of ZnO Thin Films Deposited on ITO Coated PET Substrates by RF Magnetron Sputtering under Continuous Wave Laser Regime. *Optik* **2021**, *225*, 165835. [CrossRef]
53. Jagadale, S.B.; Patil, V.L.; Vanalakar, S.A.; Patil, P.S.; Deshmukh, H.P. Preparation, Characterization of 1D ZnO Nanorods and Their Gas Sensing Properties. *Ceram. Int.* **2018**, *44*, 3333–3340. [CrossRef]

54. Khan, M.I.; Bhatti, K.A.; Qindeel, R.; Alonizan, N.; Althobaiti, H.S. Characterizations of Multilayer ZnO Thin Films Deposited by Sol-Gel Spin Coating Technique. *Results Phys.* **2017**, *7*, 651–655. [CrossRef]
55. Morales, C.; Leinen, D.; del Campo, A.; Ares, J.R.; Sánchez, C.; Flege, J.I.; Gutiérrez, A.; Prieto, P.; Soriano, L. Growth and Characterization of ZnO Thin Films at Low Temperatures: From Room Temperature to −120 °C. *J. Alloys Compd.* **2021**, *884*, 161056. [CrossRef]
56. Nunes, D.; Pimentel, A.; Santos, L.; Barquinha, P.; Pereira, L.; Fortunato, E.; Martins, R. Structural, Optical, and Electronic Properties of Metal Oxide Nanostructures. In *Metal Oxide Nanostructures*; Korotcenkov, G., Ed.; Elsevier: London, UK, 2019; pp. 59–102. [CrossRef]
57. Kumar, K.D.A.; Ganesh, V.; Shkir, M.; AlFaify, S.; Valanarasu, S. Effect of Different Solvents on the Key Structural, Optical and Electronic Properties of Sol–Gel Dip Coated AZO Nanostructured Thin Films for Optoelectronic Applications. *J. Mater. Sci. Mater. Electron.* **2018**, *29*, 887–897. [CrossRef]
58. Sharmin, A.; Tabassum, S.; Bashar, M.S.; Mahmood, Z.H. Depositions and Characterization of Sol–Gel Processed Al-Doped ZnO (AZO) as Transparent Conducting Oxide (TCO) for Solar Cell Application. *J. Theor. Appl. Phys.* **2019**, *13*, 123–132. [CrossRef]
59. Shewale, P.S.; Lee, S.H.; Yu, Y.S. Effects of Annealing Temperature of Spin-Coated ZnO Seed-Layer on UV Photo-Sensing Properties of PLD Grown ZnO: Mg Thin Films. *J. Alloys Compd.* **2019**, *774*, 461–470. [CrossRef]
60. Korotcenkov, G. Current Trends in Nanomaterials for Metal Oxide-Based Conductometric Gas Sensors: Advantages and Limitations. Part 1: 1D and 2D Nanostructures. *Nanomaterials* **2020**, *10*, 1392. [CrossRef] [PubMed]
61. Mirzaei, A.; Kim, S.S.; Kim, H.W. Resistance-Based H_2S Gas Sensors Using Metal Oxide Nanostructures: A Review of Recent Advances. *J. Hazard. Mater.* **2018**, *357*, 314–331. [CrossRef] [PubMed]
62. Huang, M.; Lian, J.; Si, R.; Wang, L.; Pan, X.; Liu, P. Spatial Separation of Electrons and Holes among ZnO Polar {0001} and {10$\bar{1}$0} Facets for Enhanced Photocatalytic Performance. *ACS Omega* **2022**, *7*, 26844–26852. [CrossRef] [PubMed]
63. Akbari-Saatlu, M.; Procek, M.; Mattsson, C.; Thungström, G.; Törndahl, T.; Li, B.; Su, J.; Xiong, W.; Radamson, H.H. Nanometer-Thick ZnO/SnO_2Heterostructures Grown on Alumina for H_2S Sensing. *ACS Appl. Nano Mater.* **2022**, *5*, 6954–6963. [CrossRef] [PubMed]
64. Kaur, N.; Singh, M.; Comini, E. One-Dimensional Nanostructured Oxide Chemoresistive Sensors. *Langmuir* **2020**, *36*, 6326–6344. [CrossRef]
65. Joshi, N.; da Silva, L.F.; Shimizu, F.M.; Mastelaro, V.R.; M'Peko, J.-C.; Lin, L.; Oliveira, O.N. UV-Assisted Chemiresistors Made with Gold-Modified ZnO Nanorods to Detect Ozone Gas at Room Temperature. *Microchim. Acta* **2019**, *186*, 418. [CrossRef]
66. Cai, Z.; Kim, K.K.; Park, S. Room Temperature Detection of NO_2 Gas under UV Irradiation Based on Au Nanoparticle-Decorated Porous ZnO Nanowires. *J. Mater. Res. Technol.* **2020**, *9*, 16289–16302. [CrossRef]
67. Han, C.; Li, X.; Liu, Y.; Li, X.; Shao, C.; Ri, J.; Ma, J.; Liu, Y. Construction of In_2O_3/ZnO Yolk-Shell Nanofibers for Room-Temperature NO_2 Detection under UV Illumination. *J. Hazard. Mater.* **2021**, *403*, 124093. [CrossRef] [PubMed]
68. Kumar, G.S.; Xuejin, L.; Du, Y.; Geng, Y.; Hong, X. UV-Light Enhanced High Sensitive Hydrogen (H_2) Sensor Based on Spherical Au Nanoparticles on ZnO Nano-Structured Thin Films. *J. Alloys Compd.* **2019**, *798*, 467–477. [CrossRef]
69. Wang, J.; Hu, C.; Xia, Y.; Zhang, B. Mesoporous ZnO Nanosheets with Rich Surface Oxygen Vacancies for UV-Activated Methane Gas Sensing at Room Temperature. *Sens. Actuators B Chem.* **2021**, *333*, 129547. [CrossRef]
70. Wang, H.; Yang, Y.; Xie, T.; Lin, Y. Highly Sensitive and Selective HCHO Sensor Based on Co Doped ZnO Hollow Microspheres Activated by UV Light. *IEEE Sens. J.* **2021**, *21*, 7558–7564. [CrossRef]
71. Wu, T.; Wang, Z.; Tian, M.; Miao, J.; Zhang, H.; Sun, J. UV Excitation NO_2 Gas Sensor Sensitized by ZnO Quantum Dots at Room Temperature. *Sens. Actuators B Chem.* **2018**, *259*, 526–531. [CrossRef]
72. Vuong, N.M.; Chinh, N.D.; Hien, T.T.; Quang, N.D.; Kim, D. and K.; Yoon, H. and; Kim, S.-G. and; Kim, D. Gas-Sensing Properties of ZnO Nanorods at Room Temperature Under Continuous UV Illumination in Humid Air. *J. Nanosci. Nanotechnol.* **2016**, *16*, 10346–10350. [CrossRef]